Lithium-Ion Glass Gating of HgTe Nanocrystal Film with Designed Light-Matter Coupling

Stefano Pierini, Claire Abadie, Tung Huu Dang, Adrien Khalili, Huichen Zhang, Mariarosa Cavallo, Yoann Prado, Bruno Gallas, Sandrine Ithurria, Sébastien Sauvage, et al.

Lithium-ion glass gating of HgTe nanocrystal film with designed light-matter coupling

Stefano Pierini[1$], Claire Abadie[2$], Tung Huu Dang[1], Adrien Khalili[1], Huichen Zhang[1], Mariarosa Cavallo[1], Yoann Prado[1], Bruno Gallas[1], Sandrine Ithurria[3], Sébastien Sauvage[4], Jean Francois Dayen[5,6], Gregory Vincent[2], Emmanuel Lhuillier[1*]

[1] Sorbonne Université, CNRS, Institut des NanoSciences de Paris, INSP, F-75005 Paris, France.
[2] ONERA - The French Aerospace Lab, 6, chemin de la Vauve aux Granges, BP 80100, 91123 Palaiseau, France.
[3] Laboratoire de Physique et d'Etude des Matériaux, ESPCI-Paris, PSL Research University, Sorbonne Université Univ Paris 06, CNRS UMR 8213, 10 rue Vauquelin 75005 Paris, France.
[4]Université Paris-Saclay, CNRS, Centre de Nanosciences et de Nanotechnologies, 91120, Palaiseau, France.

[5] Université de Strasbourg, IPCMS-CNRS UMR 7504, 23 Rue du Loess, 67034 Strasbourg, France
[6]Institut Universitaire de France, 1 rue Descartes, 75231 Paris cedex 05, France

Abstract: Nanocrystals (NCs) band gap can be easily tuned over the infrared range, making them appealing for the design of cost-effective sensors. Though their growth has reached a high level of maturity, their doping remains a poorly controlled parameter raising the need for post-synthesis tuning strategies. As a result, the phototransistor device geometry offers an interesting alternative to the photoconductor one, allowing carrier density control. Phototransistors based on NCs targeting integrated infrared sensing have to (*i*) be compatible with low-temperature operation, (*ii*) avoid liquid handling, and (*iii*) enable large carrier density tuning. These constraints drive the search for innovative gate technologies beyond traditional dielectric or conventional liquid and ion gel electrolytes. Here, we explore lithium-ion glass gating and apply it to channels made of HgTe narrow band gap NCs. We demonstrate that this all-solid gate strategy is compatible with large capacitance up to 2 µF.cm^{-2} and can be operated over a broad range of temperatures (130-300 K). In the last part of the paper, we tackle an issue often faced by NCs-based phototransistors, which is their low absorption: from a metallic grating structure, we combined two resonances and achieved a high responsivity (10 A.W^{-1} or external quantum efficiency of 500 %) over a broadband spectral range.

Keywords: field effect transistor, solid electrolyte, HgTe, nanocrystals, nanophotonics, light resonator, infrared detection.

[$] authors have equal contributions.

*To whom correspondence should be sent: el@insp.upmc.fr

1. Introduction

As colloidal growth of nanoparticles has gained maturity, nanocrystals (NCs) have become viable building blocks for optoelectronics. Using narrow band gap materials, it is possible to address the infrared (IR) part of the electromagnetic spectrum[1,2]. At such wavelengths, NCs offer an interesting alternative to epitaxially grown semiconductors to design cost-effective devices.[3] This has led to the demonstration of efficient light-emitting devices[4–7] as well as effective light sensors,[8–10] including focal plane arrays used to image near and mid-IR light.[11,12]

Though a high degree of control is achieved for the growth of this material, its doping remains[13] a challenge, and the material may not behave as an intrinsic semiconductor. This affects the final device performance. Thus, it is of utmost interest to couple NCs films with a gating method to enable an agile tunability of the carrier density. As a result, the phototransistor appears to be a remarkable evolution of the photoconductive geometry since the gate bias can be used as a knob to control the magnitude of the dark current. Phototransistors are built around a field-effect transistor[14] (FET) in which, in addition to drain/source electrodes and a channel based on a NC film, the gate appears as a central building block. The gate is used as a capacitor and, applying a bias over it, it generates charges tuning the carrier density in the FET channel.

Various technologies of gates have been coupled to NCs films.[15] The most conventional method continues to rely on dielectrics such as SiO_2.[9,16,17] The latter being commercially available and technologically mature, it presents the clear benefit of being easy to implement. Moreover, the fast gate bias sweep and the ability to operate at low temperatures are other key advantages of this technology. The low dielectric constant of silica, on the other hand, requires a large bias operation, possibly close to the material breakdown. High-k materials such as alumina, ZrO_x [18,19] or HfO_2 are the natural alternatives.[20–23] They present the advantage of an all-solid strategy similar to silica but require an additional fabrication step with the deposition of an insulating layer. Despite a limited number of examples,[19,20] ferroelectric gating coupled to a NC film offers a strategy to achieve even higher capacitance FETs[19,20]. The main idea behind ferroelectric gating is to take advantage of the divergence of a ferroelectric material's dielectric constant close to its Curie temperature. However, the latter limitation tends to reduce the operating temperature ranges. When higher gate capacitances are required, the gating methods based on ion displacement become the most effective. Contrary to the previous methods, electrolytes allow for bulk gating. This ability to gate a thick film is critical for the design of phototransistors, which require a film thickness suitable with the light absorption depth.[26,27] The electrolyte is already commonly used to control the carrier density of a NC population.[28–30] The usual method is to introduce liquid or ion gel electrolyte, which may bring additional constraints related to liquid handling and moisture sensitivity: this is why a solid electrolyte appears easier to implement. The use of ionic glasses has been a step in this direction: LaF_3 glass presents, for example, mobile fluoride vacancies which can be used to induce gating.[31–33]

When applied to infrared phototransistors, the gate has to fulfill some specific constraints such as being (*i*) compatible with operations below room temperature, (*ii*) solid state-based to be conveniently integrated into a device, and finally (*iii*) associated with a large capacitance to tune the relatively large thermally activated carrier density observed in narrow band gap NCs. In this perspective, new materials compatible with this series of constraints must be identified. For a long time, the battery field was using solid electrolytes, and their potential for field-effect transistors has been investigated for 2D materials[34–37] and superconductor based[38] FETs, but they remain unused for NC-based FETs. Here, we explore the potential of this strategy to design a FET based on HgTe NCs[39] presenting an absorption in the extended short-wave infrared. We show in particular that this lithium-ion glass substrate tends to promote hole injection over electron injection compared to what is observed with a silica gate. In the last part of the paper, we propose an update of the design to engineer the light-matter coupling in this system and achieve high absorption from

a thin NC film. This strategy allows a large responsivity (R>10 $A.W^{-1}$), three orders of magnitude larger than the value obtained without a light management strategy.

2. Materials and methods

2.1. Nanocrystals growth

Chemicals: Mercury chloride ($HgCl_2$, Sigma-Aldrich, 99%), **Mercury compounds are highly toxic. Handle them with special care.** tellurium powder (Te, Sigma-Aldrich, 99.99%), trioctylphosphine (TOP, Alfa Aesar, 90%), oleylamine (OLA, Acros, 80-90%), dodecanethiol (DDT, Sigma-Aldrich, 98%), ethanol absolute anhydrous (VWR), methanol (VWR, >98%), isopropanol (IPA, VWR), hexane (VWR, 99%), 2-mercaptoethanol (MPOH, Merck, >99%), N,N dimethylformamide (DMF, VWR), toluene (VWR, 99.8 %), acetone (VWR), methylisobutylketone (MIBK, VWR, >98.5%)

All chemicals are used without further purification except oleylamine that is centrifuged before use.

1 M TOP:Te precursor: 2.54 g of Te powder is mixed in 20 mL of TOP in a three neck flask. The flask is kept under vacuum at room temperature for 5 min and then the temperature is raised to 100 °C. Furthermore, degassing of flask is conducted for the next 20 min. The atmosphere is switched to nitrogen and the temperature is raised to 275 °C. The solution is stirred until a clear orange coloration is obtained. The flask is cooled down to room temperature and the color changes to yellow. Finally, this solution is transferred to a nitrogen filled glove box for storage.

HgTe NCs synthesis with band-edge at 4000 cm^{-1}: In a 100 mL three neck flask, 543 mg of $HgCl_2$ and 50 mL of oleylamine are degassed under vacuum at 110 °C. Meanwhile, 2 mL of TOP:Te (1 M) are extracted from the glove box and mixed with 8 mL of oleylamine. After the atmosphere is switched to N_2 and the temperature stabilized at 82 °C, the TOP:Te solution is quickly injected. After 2 min 30 s, 10 mL of a mixture of DDT in toluene (10% of DDT) is injected and a water bath is used to quickly decrease the temperature. The content of the flask is split over 4 centrifuge tubes and MeOH is added. After centrifugation, the formed pellet is redispersed in one centrifuge tube with toluene. The solution is precipitated a second time using ethanol. Again, the formed pellet is redispersed in toluene. At this step the CQDs are centrifuged in pure toluene to get rid of the lamellar phase. The solid phase is discarded. The stable phase is transferred in a weighted centrifuge tube and finally precipitated using methanol. The solid is dried under vacuum for 30 min (in glove box vacuum chamber). Finally, CQDs are redispersed with a 50 $mg.mL^{-1}$ concentration in toluene.

HgTe ink: We dissolve 30 mg of $HgCl_2$ in a solution of 18 mL of DMF and 2 mL of mercaptoethanol. The original solution of HgTe tripods nanoparticle is treated to obtain ligand exchange. At each step the solution is stirred with a vortex and sonicated. 900 µL of HgTe nanocrystal solution at 50 $mg.mL^{-1}$ are mixed with 1 mL of the exchange solution. 5 mL of hexane and 2 mL of DMF are added to the solution. The top phase is then removed, and the solution is washed three more times adding 5 mL of hexane and removing the top phase each time. Finally, toluene is added up to reach a global volume of 4 mL and the solution is centrifugated for 2 min at 6000 rpm to precipitate the nanoparticles. The supernatant is discarded and the formed pellet is dried using nitrogen flux and then redispersed in 175 µL of DMF in order to target a thickness of about $100\ \mathrm{nm}$. The obtained solution is called ink. Before ink deposition, the substrate is placed in an oxygen plasma cleaner for 2 min to promote adhesion. The ink is spin-coated on the substrate at 4000 rpm (with $2000\ \mathrm{rpm} \cdot \mathrm{s}^{-1}$ acceleration) for 1 minute. This gives a homogeneous film between 100 nm and 250 nm, as can be

seen in the height profile obtained from the profilometer. The speed of spin coating and ink concentration are used to tune the film thickness.

2.2. Material characterization

Infrared spectroscopy: For infrared spectroscopy, we use a Fischer Nicolet iS50 in attenuated total reflection (ATR) mode. The spectra are averaged over 32 acquisitions and have a 4 cm^{-1} resolution. For photocurrent spectra, the sample is biased using the supply from a Femto DLPCA 200 current amplifier, the current is then magnified by the same amplifier and the output of the latter is fed into the electronic of the FTIR. For polarized measurements a polarizer, aligned with the electrode digits (or perpendicular to them) is added on the optical path. Background is then acquired in presence of the polarizer in both polarizations.

Transmission electron microscopy: A drop of the NC solution is drop-casted onto a copper grid covered with an amorphous carbon film. The grid is degassed overnight to reduce future.

2.3. Electrical characterization

Electrode fabrication: the solid electrolyte is purchased from MTI (ref EQ-CGCS-LD). It is a ceramic based on Li_2O-Al_2O_3-SiO_2-P_2O_5-TiO_2. The substrate is cleaned with acetone and rinsed with ethanol and isopropanol, before being dried by a nitrogen jet gas. First LOR 3A, a sacrificial release layer is spin-coated and baked at 160°C for 180 seconds. Then, AZ 1505 resist is spin-coated and annealed at 105 °C for 90 seconds. A laser lithography (Heidelberg µPG 101) is used to perform the lithography procedure. The resist is developed in a solution of AZ 726 for 20 s, and then rinsed in deionized water. Then 3 nm of Ti and 47 nm of Au are evaporated using an e-beam evaporator (plassys MEB 550s). For lift-off the substrate is dipped in a PG remover bath for 1 h and finally rinsed using DI water. The substrate is then dried and electrically tested to check that there is no electrical short. The electrodes are interdigitated electrodes as schematized in **Erreur ! Source du renvoi introuvable.** with 25 pairs of digits (*i.e.,* 49 spacings). Each digit is 700 µm long and spaced from its neighbor by 10 µm.

Electrical measurements: The drain and source contacts of the sample are cleaned using a cotton swab moistened with acetone. The sample is glued using a silver paste on a substrate of silicon covered with a gold layer and mounted on the cold finger of a cryostat. The gold layer is used as gate.The transfer curves and the IV curves are measured using a Keithley 2634B SourceMeter; that controls both the gate-source and the drain-source voltages, measuring the relative currents.

Photocurrent measurements: The time response measurements and the responsivity measurements are performed using the scope mode of a MLFI Lock-In Amplifier (Zurich Instruments). In this case both the drain-source and the gate-source voltages are controlled by the Lock-In amplifier. **Erreur ! Source du renvoi introuvable.** schematized the setup used for the responsivity measurements. A wavefunction generator is used to trigger the laser emission and the oscilloscope, the current is converted in voltage by the Femto DLPCA-200 amplifier and fed into the oscilloscope (Tektronix MDO 3102). From the time trace we can extract both the photocurrent amplitude and the time response.

Impedance Measurements: The MLFI Lock-In Amplifier (Zurich Instruments) is used to perform impedance measurements in the range from 0.1 Hzto 500 kHz. We used an AC voltage of 100 mV. No DC voltage was applied exploring the temperature dependence of the impedance. We first

deposit two gold layers on both sides of a Li-based substrate. The surface of the deposited gold layer is determined a posteriori using a camera and digital processing of the image. The area of the device is 8.9 mm^2. The device is glued on a substrate of silicon coated with a gold layer using silver paste. The sample is then connected inside the cryostat, the top and the back sides are connected to the Lock-In amplifier.

Noise measurement. Current from the device (at 0.7 V bias, kept in the dark) is amplified by a Femto DLPCA-200, then fed into a SRS SR780 spectrum analyzer. The sample is mounted on the cold finger of a close cycle cryostat.

Detectivity determination. The specific detectivity (in Jones) of the sample is determined using the formula: $D^* = \frac{R\sqrt{A}}{S_I}$, where R (in $A.W^{-1}$) is the responsivity, S_I is the noise ($A/\sqrt{Hz}$) and A the area of the device (cm^2).

2.4. Optical resonator

Determination of the optical index: We used spectrally resolved ellipsometry to determine the complex optical index of the different materials involved in the device and later conduct electromagnetic simulations.

Spectroscopic ellipsometry: The spectroscopic ellipsometry measures the change in the polarization state between the incident and the reflected light and this is done by measuring the angles ψ and Δ. The following relation applies:

$$\rho = \frac{r_p}{r_s} = \left|\frac{r_p}{r_s}\right| e^{i(\delta_p - \delta_s)} = \tan\psi\, e^{i\Delta}$$

where r_p and r_s are the reflection coefficients of p and s polarized light respectively and where δ_p.and δ_p are the phase shifts in reflection in p and s polarizations, respectively. The measurements are performed on a V-VASE ellipsometer (J.A. Woollam) in the 500-2000 nm range with steps of 10 nm and with angles of incidence of 50°, 60° and 70°. For the Li based substrate, the real part is shown in **Erreur ! Source du renvoi introuvable.** and is later used as a free parameter to fit experimental data and we found that n=1.8 gives a reasonable fit as shown in Figure 4c. To account for the diffusive character of the substrate we use k=1 for the substrate.
Complementarily, note that for gold complex optical index, we have used ref [40]. **Erreur ! Source du renvoi introuvable.** provides the imaginary part of the complex optical index of the HgTe NC film. The real part of the optical index has been taken constant and equal to 2.2 according to ref [41].

Electromagnetic simulation: Simulations are conducted using COMSOL, a software using Finite Element Method. The array of resonators is modelled using RF module in 2D geometry. It is one unit cell and Floquet periodic boundary conditions are used to describe the periodicity. On both sides (top and bottom), we define perfectly matched layers (PML) to absorb all outgoing waves and prevent nonphysical reflections. The absorption comes from emw. Qe, a value corresponding in COMSOL to the power density dissipated in $W.m^{-3}$. In air there is no diffracted order for wavelengths above the electrode period. For shorter wavelengths, the energy propagating in the diffracted orders is absorbed by PML. On top of the resonator inside air, a port condition is used to define the incident wave, either in TE or TM polarization. An automatic mesh was used in these simulations with a predefined “Extremely fine” mesh, which means that the maximum element size is 140 nm, except for the PML where a mapped mesh is used with a distribution of 12 elements.

To enhance the device absorption, we keep the same device geometry as the one depicted in **Erreur ! Source du renvoi introuvable.** and just update some geometrical factors, see **Erreur ! Source du renvoi introuvable.**. We tune the period, the size of the digit and the film thickness so that light absorption resonances are generated. Along the TE polarization we design a guided mode resonance. This mode is dispersive and split in two modes with angle as revealed by the dispersion map along the TE polarization **Erreur ! Source du renvoi introuvable.**a. In TM mode, we observe one main resonance that we design to be red shifted compared to the TE mode. This mode is non dispersive, see TM dispersion map in **Erreur ! Source du renvoi introuvable.**b, and while it is not affected by the digit size (*i.e.* no shift of the resonance peak for various digit sizes, see **Erreur ! Source du renvoi introuvable.**), it can strongly be affected by the film thickness (*i.e.* strong shift of the resonance peak away from the exciton peak, see **Erreur ! Source du renvoi introuvable.**) which suggests a vertical Fabry-Pérot resonance.

Fabrication of the device with resonator The fabrication of the optimized photoresponsive device is made in two steps of lithography. First the main contact pads are fabricated using optical lithography and then the interdigitated pattern is fabricated using e-beam patterning.

Electrodes for electrical contacts: A lithium-ion glass substrate is initially rinsed with acetone and isopropanol to remove dust and organic contaminants. An additional O_2 plasma cleaning step is performed for 5 minutes. The TI Prime adhesion promoter is spin-coated onto the substrate and baked on a hot plate at 120 ºC for 2 minutes. Subsequently, the substrate is spin-coated with AZ5214E photoresist and baked at 110 ºC for 1 minute 30 seconds. The first UV exposure through a mask is 1 second as the substrate is very strongly scattering light and this is followed by the image reversal bake step at 125 ºC for 2 minutes. A flood exposure for 40 seconds without the mask is then performed. The resist film is developed in AZ726 MIF with a development time of 30 seconds, followed by DI water rinse, N_2 gun and finally an oxygen plasma of 5 minutes. The next step is to deposit 5 nm of Cr and 80 nm of Au on the substrate with a thermal evaporator. Afterwards, the substrate stays 2 hours in acetone for lift-off. The obtained pattern is shown **Erreur ! Source du renvoi introuvable.**a.

Fabrication of gold nano-stripes: We use Raith eLine e-beam lithography system for the fabrication of the nano-stripes. First, a 400 nm thick PMMA layer is spin-coated onto the substrate patterned with macroscopic electrodes. The resist is then baked at 180 ºC for 2 minutes. We deposit 10 nm of Al with a thermal evaporator in order to reduce the charging effect. The operating bias of the electron beam is set to 20 kV, and the aperture is set to 10 µm. The dose is set to 170 µC/cm^2. The resist is first dipped during 15 seconds in a KOH solution in order to remove the aluminum layer and then it is developed in a solution of MIBK:isopropanol (1:3 in volume) for 45 seconds and rinsed with isopropanol. An oxygen plasma of 5 minutes is done to remove traces of resist. 5 nm Cr and 80 nm Au are then deposited with a thermal evaporator. The substrate stays in hot acetone (45°C) for 2 hours after letting it overnight for lift-off. The obtained pattern is shown in **Erreur ! Source du renvoi introuvable.**b-d.

For resonator measurements a thicker film compared to transistor measurements was needed (>200 nm). Thicker films can be obtained mostly by updating the spin coating condition which is conducted at reduced speed. The ink is spin-coated on the substrate at 1500 rpm (at 500 rpm.s^{-1} acceleration) during 5 minutes (after initial DMF deposition on the substrate with the same speed in order to help adhesion) followed by a fast spin coating step to dry edges (3000 rpm for 2 min, with 500 rpm.s^{-1}). This gives a homogeneous deposition around 225 nm, see **Erreur ! Source du renvoi introuvable.** for an image of the electrode after functionalisation with the NC film.

3.Results and discussion

3.1 Material of interest with short wave infrared band gap

To design a short wave-infrared (SWIR) absorbing phototransistor, we proceed in two informative steps. In the first step, we rely on a doped silica substrate. We use HgTe NCs as the material for the FET channel. The nanocrystals are obtained using the Keuleyan's procedure.[42] HgTe NCs present a tripodic shape according to electronic microscopy (**Figure 1**b) and a band edge at 2 µm with a cut-off wavelength around 2.5 µm, see the absorption spectrum in **Figure 1**a. In addition of the electronic interband transition attributed to HgTe, the absorption spectrum depicts a doublet that is attributed to the C-H bond resonance at around 2900 cm^{-1}. Several steps of cleaning are conducted in order to reduce the relative magnitude of the C-H resonance close to the one of the NC exciton. When a similar magnitude is obtained, thin conductive and photoconductive films of such NCs are obtained by preparing an ink.[16,43] In this case, the native insulating long ligands (dodecanethiol) are stripped off and replaced by a mixture of a short thiol (mercaptoethanol) and ions ($HgCl_2$) dissolved in dimethylformamide (DMF). The obtained ink can be spin-coated to form a thin film. The film thickness can be tuned with the deposition conditions in the 100 to 300 nm range for the device under investigation in this study.

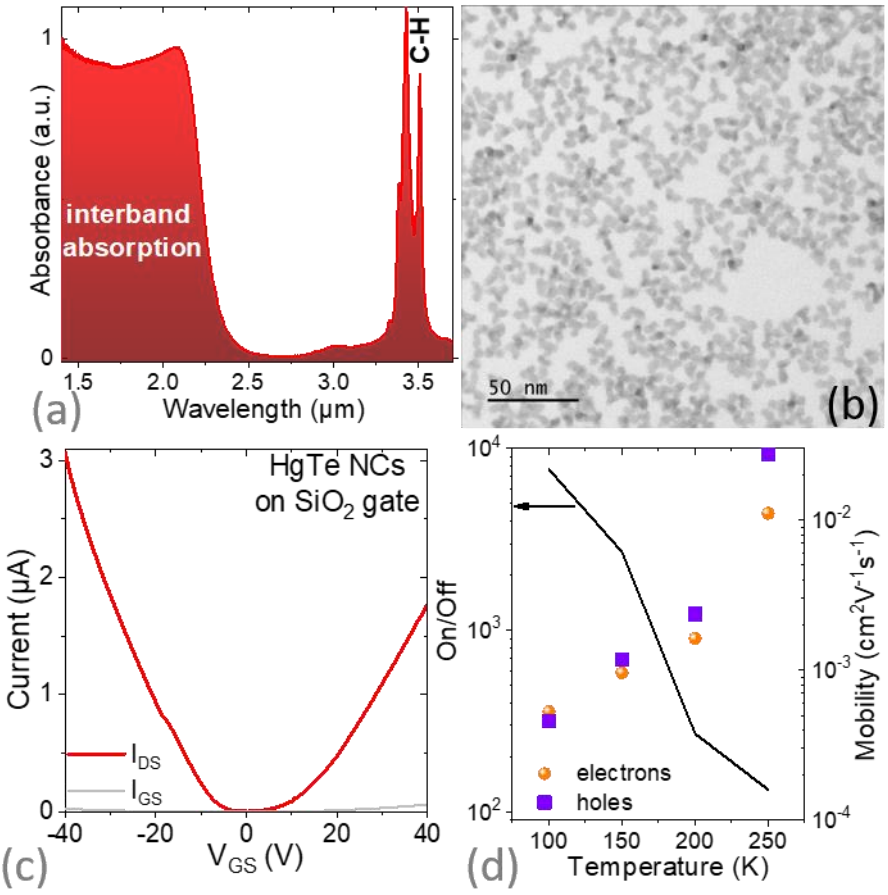

Figure 1 *a. Absorption spectrum of the HgTe NCs measured in attenuated total reflexion mode. The doublet at around 3.4 µm is related to the resonance of the C-H bond. b Transmission electron microscopy image of the HgTe NCs. c. Transfer curve (drain and gate current as a function of applied gate bias under the constant drain-source bias of 100 mV), measured at 150 K, for a field-effect transistor which channel is made of a HgTe NC film while the gate is SiO_2 (300 nm SiO_2 on top of highly doped Si). d. On/Off ratio and carrier mobility as a function of the temperature for a FET which channel is made of HgTe NCs and the gate of 300 nm SiO_2.*

Once deposited on a doped Si/SiO_2 substrate on which gold interdigitated electrodes have been fabricated, the material presents an ambipolar character. We observe both holes (under negative bias) and electrons (under positive gate bias), as shown in the transfer curve, see **Figure 1**c. The current modulation is around two orders of magnitude at 250 K and increases to almost four decades at 100 K, see **Figure 1**d. This increase in current modulation is mostly due to a reduction in the off current caused by reduced carrier density activation when the temperature drops.

The carrier mobility can be determined from the transfer curve with $\mu = \frac{L}{WC_\Sigma V_{DS}} \frac{\partial I_{DS}}{\partial V_{GS}}$, where *L* is the electrode spacing (10 µm), W is the electrode length (49 × 2.5 mm), C_Σ the surface capacitance as measured in **Figure 2**b and V_{DS} the drain source bias. We notice a clear thermal activation of the mobility (**Figure 1**d) which is consistent with the hopping conduction occurring in a disordered array of polydisperse NCs. Electron and hole mobilities are similar in magnitude and drop by a factor 50 as the temperature is reduced from 250 to 100 K.

3.2 Gating using solid electrolyte

In the second step, we design a FET using a lithium-ion glass substrate. The latter is commercially available from MTI and is a ceramic of oxide materials (Li_2O-Al_2O_3-SiO_2-P_2O_5-TiO_2) in which the small Li^+ cations can be displaced under the application of a gate bias. On such substrates, we fabricate the same set of interdigitated electrodes as the one used for silica gating, see a schematic of the device in **Figure 2**a and S2. The benefit of such gates is best revealed by impedance measurements, see **Figure 2**b. At high frequency, the capacitance is low. In this regime, ions cannot move, and only the dielectric behavior of the substrate is observed. The substrate being thick (several hundred µm), the resulting capacitance is even weaker than in thin silica films. At low frequency, on the other hand, ions can move to form an ionic interfacial layer, and the obtained capacitance becomes high (up to 2 $\mu F.cm^{-2}$). The transition frequency between these two regimes depends on the temperature and reflects the thermally activated transport of Li^+ ions within the substrate. In practice, ion displacement limits the gate sweep rate range, and the strongest modulations are obtained with low bias sweep rates (1 $mV.s^{-1}$ typically, see **Figure 2**e). Note that the capacitance value obtained is similar to the one obtained with a liquid or ion gel electrolyte, while the device can be air-operated without handling any liquid.

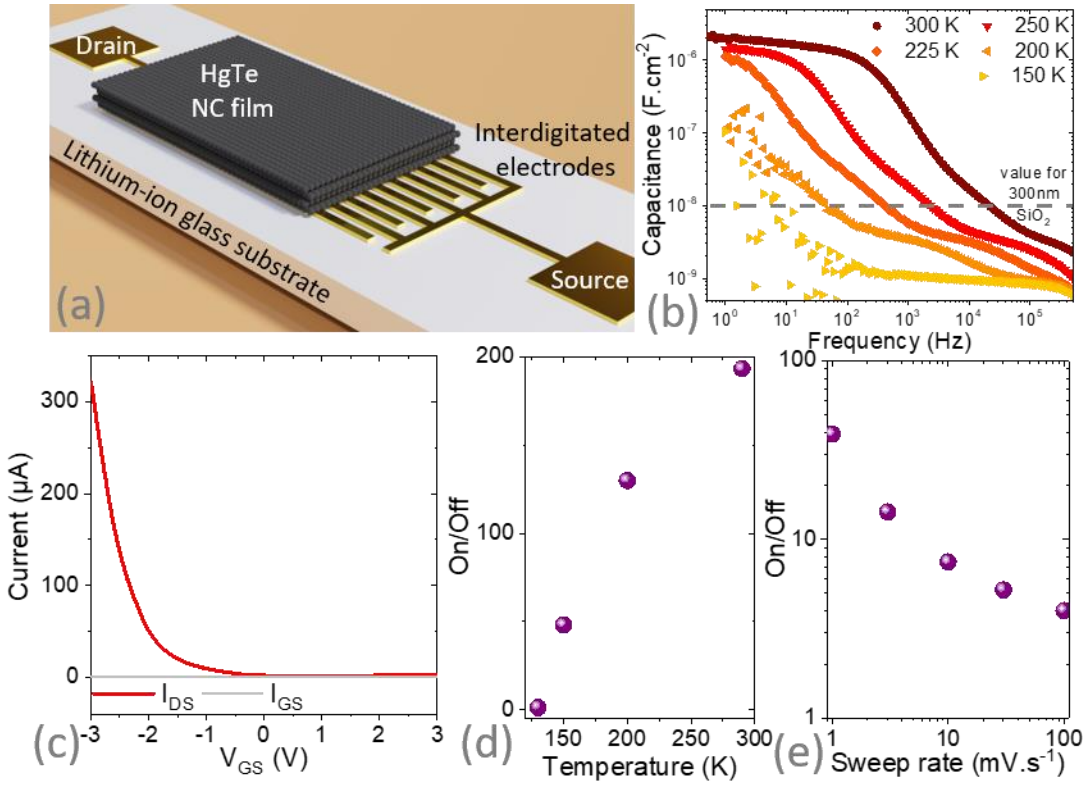

Figure 2*a. Schematic of the FET which channel is made of HgTe NC film and the gate is made of a lithium-ion glass substrate. The substrate is used as gate and the gate electrode is taken on the back side of the substrate. b. Capacitance of the lithium-ion glass substrate as a function of the signal frequency for various temperatures. c. Transfer curve for the FET depicted in part a, at room temperature (V_{DS}= 500mV). On/Off ratio (i.e. ratio of the maximum current over the minimul current in the tranfer curve) for the same FET as a function of temperature (d) and gate bias sweep rate at 200 K (e).*

As bias is applied over the lithium-ion glass substrate, current modulation is observed in the HgTe NC film, see **Figure 2**c and S3-4. Current modulation is observed for temperatures down to 130 K (see **Figure 2**d); below this value, ions freeze. This enables the operation of the FET from room temperature down to this value, which is a broader range than the typical one of liquid electrolyte (acetonitrile often used as solvent freezes at -45°C) or ionic glass[31–33] (operating range 180-300 K). However, despite the higher capacitance than with silica, the on off ratio is not improved due to higher leakage inherent to the gating method based on ions displacement.
A striking feature is the observation of *p*-type only conduction (**Figure 2**c), whereas the material was ambipolar when coupled to silica gate. This means that the lithium-ion glass substrate behaves as a carrier selective charge injector. This behavior likely results from an asymmetry in the mobility of Li^+ cations and their vacancies in the lithium-ion glass substrate. We have estimated the hole mobility at 250 K to be $6x10^{-3}$ $cm^2.V^{-1}.s^{-1}$. This is typically 3 times lower than the value measured for SiO_2 gate, this reflects a carrier density dependence of the mobility.

The purpose of this device being its use as a phototransistor, we tested its potential under illumination at 1.55 µm. As expected for such NCs films, the material is photoresponsive and we observe a responsivity around R=5 $mA.W^{-1}$ (floating gate) which can be tuned by applying a gate bias, see **Figure 3**a. Though higher responsivity (up to R=11 $mA.W^{-1}$) can be obtained under negative gate bias, the strongest photocurrent modulation is obtained under positive gate bias since this operating condition makes the material more intrinsic. As often observed in NC-based phototransistors, the change of the photocurrent magnitude comes with a change of the response

dynamics[27], see **Figure 3**b. Faster responses are obtained, when majority carriers are removed (*i.e.,* positive gate bias here). These changes in dynamics reflect the change in trap filling when the gate bias is applied[44]. With Li gating, the response time spans from 500 µs to 5 ms depending on the applied gating bias. The former value is itself a decade longer than the value obtained with the silica gate, also associated with a much weaker photoresponse. In other words, the FET configuration enables to tune the device photoresponse while leaving the gain bandwidth product almost unaffected.

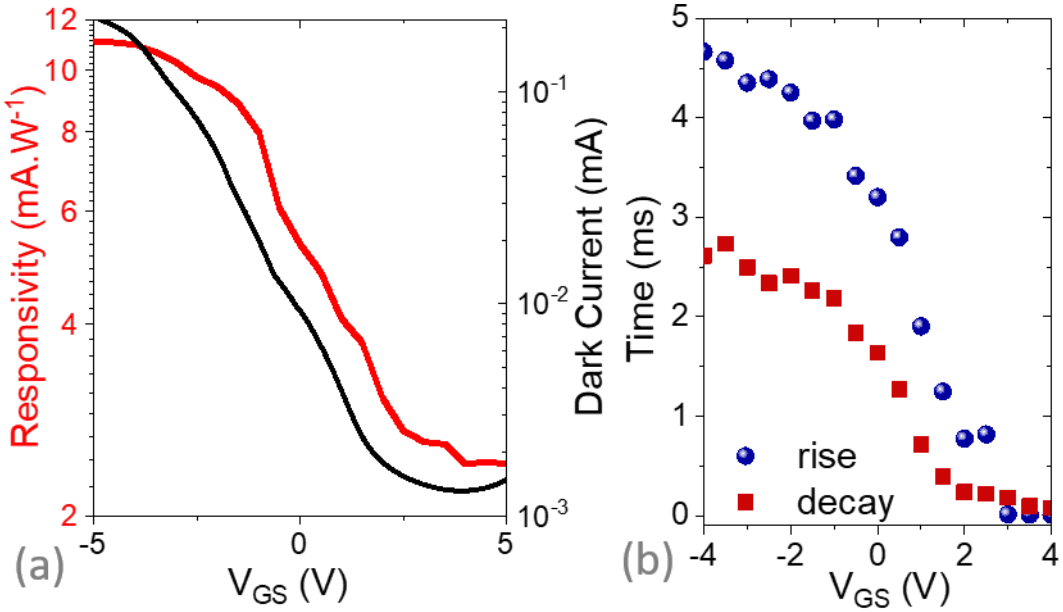

Figure 3*a. Dark current and responsivity for a device depicted in* ***Figure 2****a as a function of the applied gate bias. b. Rise and decay time (defined as the time for the signal to change from 10 % to 90 % of its final value) as a function of applied gate bias, see Figure S 5 for a time trace. Illumination is ensured by a 1.55 µm laser diode at 110* $mW \cdot cm^{-2}$*, spectra are averaged 500 times The drain-source bias is set at 500 mV. Measurements are conducted at 250 K.*

3.3 Introduction of a photonic structure to enhance the absorption

As most NC-based light sensors in this configuration, the device faces a limitation. Due to hopping conduction, the mobility and the diffusion length are limited. As a result, the effective light absorption only occurs over a distance much shorter than the light absorption depth (>µm for HgTe NC in the SWIR[45]). Electromagnetic simulations reveal that the film absorbs around 10% of the incident light at the NC band edge. To overcome this limitation, we update the design of the device to couple the NCs to a photonics structure,[46] while maintaining the same interdigitated geometry (Figure S6). The initial device relies on interdigitated electrodes with 10 µm wide digits and 10 µm spacing between digits. We then tune the geometrical factors (film thickness, period and size of the digits) in order to maximize the absorption in magnitude and linewidth. Compared to the previous work by Gréboval *et al*[20] also dealing with a phototransistor coupled to a light resonator, the change in substrate from a single crystal of $SrTiO_3$ to a Li based ceramic which strongly scatters light (Figure S4-5) raises the need for an additional design.

We first match a resonance in the TM polarization (magnetic field parallel to the electrodes ribbons) with the band-edge energy. This first resonance, at 2.2 µm, is a vertical Fabry-Perot resonance highlighted by its lack of dispersion (see figure S7b). The energy of this resonance is driven by the film thickness (Figure S8b) but is very weakly affected by the digit width (Figure S9). The obtained mode is spatially located on top of the gold pad (**Figure 4**c) as the cavity is formed between the gold and the air interface. By doing so, we minimize the loss in the metal which is estimated to be around

5.5 % of the total absorption. Details about the electromagnetic design can be found in the supporting information.

Furthermore, by tuning the period of the grating we can induce a second resonance in TE polarization (electric field parallel to the electrodes ribbons). We choose the period of the grating and digit size to slightly blue-shift this resonance with respect to the band edge (around 1.75 µm). By doing so, we broaden the global response of the device. This mode is a guided mode resonance[47–49] (GMR), which energy is driven by the period of the grating. This mode is dispersive, as revealed by the dispersion map, see figure S7a, and spatially located at the top of the gold electrode as revealed by the simulated absorption map (**Figure 4**a). The obtained absorption within the NCs (*i.e.* leading to the generation of photocurrent) is expected to reach 40% for non-polarized light, see **Figure 4**c.

The period of the grating being set at 1.5 µm for a 750 nm wide digit, we use e-beam lithography for its fabrication, see Figure S10. The obtained photoresponse spectrum is now strongly polarized, see **Figure 4**c, with a TE mode clearly blue shifted with respect to the TM mode. Compared to the simulation, the photocurrent presents a good match both in energy and linewidth as long as we account for the scattering of the Li substrate. It is worth noting that the photocurrent spectrum is also significantly redshifted from the absorption shown in **Figure 1**a. This shift is the combination of two effects: (i) first we have conducted a ligand exchange procedure that tends to increase inter NC coupling and leads to a redshift. In addition (*ii*), the photocurrent is measured at low temperature (180 K), while HgTe NC band gap redshifts upon cooling.[45,50]

The responsivity of the device is now much higher and reaches $10\ \mathrm{A}\cdot\mathrm{W}^{-1}$ (**Figure 4**d and S14) under moderate electric field: this value is three orders of magnitude larger than the one reported for the same film deposited on conventional interdigitated electrodes without resonances. As it has already been pointed out by Chu *et al*.,[49] the enhanced responsivity splits into two contributions: absorption enhancement is responsible here for a factor 4 in the performance increase; the remaining factor 250 is due to photogain [51] (*i.e.* recirculation of one of the carriers, while the other one stays trapped). Indeed, the external quantum efficiency of the device is around 500% (R=10 $A.W^{-1}$ for 2.5 µm cut-off wavelength and under broadband blackbody radiation),

In a nanocrystal array, charge transport occurs through hopping. Under illumination, electron hole pairs get generated and one carrier can easily get trapped while the second one is transported to the electrode. To ensure the sample neutrality, the electrode will reinject this carrier that can recirculate several times until the trapped charge gets recombined.[52] The gain magnitude is the ratio of the trapped carrier lifetime to the transit time. The latter is directly connected to the device size. Thus a smaller device favors gain.[53]

The factor 250 for the gain value is further subdivided into a factor 10 that arises from an increase in the electric field (*i.e.,* a 10 times narrowing of the electrode spacing) and a factor 25 that we ascribe to a more efficient hopping transport as the device size approaches the diffusion length[49]. Noise in this device is limited by a *1/f* contribution,[54,55] see the inset of **Figure 4**e, which currently limits the detectivity around $D^*\approx 5\times10^9$ Jones and corresponds to a noise equivalent power (NEP) at around 1 $pW.Hz^{-1/2}$ for a signal at 1 kHz. This is nevertheless a factor 5 ($D^*=10^9$ jones) above the value obtained for the same material (same band gap and same surface chemistry) without resonator compared to that achieved for silica[49].

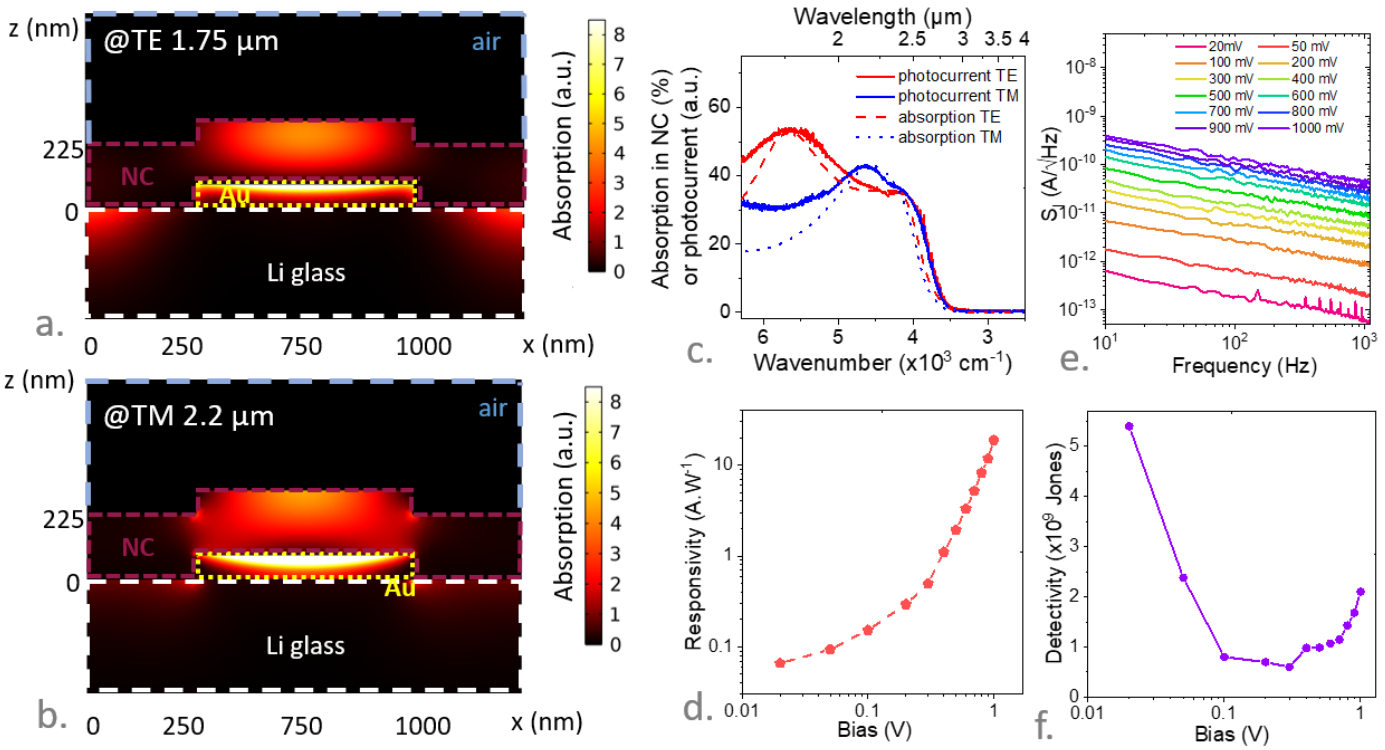

Figure 4 *a. (resp b.) Simulated absorption map at the resonance of the TE @1.75 µm (resp TM at 2.2 µm) polarization. c. Simulated absorption (dashed lines) and experimental photocurrent (solid lines) spectra within the NCs film (i.e., excluding losses in contact) for TE, TM polarization. d. Responsivity measured at 180 K for a signal at 1 kHz as a function of applied bias for the device with light resonators under broadband radiation resulting from a blackbody at 980°C. e. Noise current spectral density as a function of signal frequency measured under various applied biases. f. Specific detectivity measured at 180 K (for a signal at 1 kHz) as a function of applied bias for the device with light resonators.*

4. Conclusions

To summarize, we have demonstrated that the lithium-ion glass substrate can be used as an all-solid back gate for NC-based FET. This gate leads to a capacitance as high as 2 µF.cm^{-2}, similar to liquid electrolyte while considerably easing the device's manipulation and its future integration. Moreover, the gating remains effective over a broad range of temperatures from room temperature down to 130 K, matching the targeted operating temperature range for short- and mid- wave infrared sensors. Interestingly the gating favors hole injection compared to silica gating. In a second step, we demonstrate a light management strategy for a phototransistor based on this lithium-ion glass. We demonstrate the combination of two light resonators, one based on a guided-mode resonance and the second one relying on a Fabry-Perot mode. This combination of two resonances enables broad band enhancement in light absorption and responsivity as high as 10 A.W^{-1}, this value is a thousand times larger than the one obtained for interdigitated electrodes without any light management strategy. This enhancement can be split over a factor of 4 for absorption and a factor of 250 for photogating.

ASSOCIATED CONTENT

Supporting Information include (*i*) procedure for NC synthesis and characterization, (*ii*) additional details relative to transport and phototransport measurements, (*iii*) design of the resonator with electromagnetic simulations and device fabrication, (*iv*) additional device performances

COMPETING INTEREST

The authors declare no competing interest.

AUTHOR CONTRIBUTIONS

J.-F. D fabricated the electrodes without resonators, C.G., A.K., H.Z. and M.C. built the setups for optoelectronic characterization, S.P., C.G. conducted the FET characterization. Y.P. and S.I. grew the nanoparticles, C.A. and B.G. conducted ellipsometry measurements. CA, T.H.D. and G.V. designed the light resonators and fabricated them. E.L. and S.S. designed, funded the project and wrote the paper with input of all authors. All authors proofread the manuscript.

FUNDING

The project is supported by ERC grant blackQD (grant n° 756225) Ne2Dem (grant n° 853049) and AQDtive (grant n°101086358). We acknowledge the use of clean-room facilities from the “Centrale de Proximité Paris-Centre” and from STnano platform. This work has been supported by the Region Ile-de-France in the framework of DIM Nano-K (grant dopQD). This work was supported by French state funds managed by the ANR within the Investissements d'Avenir programme under reference ANR-11-IDEX-0004-02 and Labex NIE (ANR-11-LABX-0058, and ANR-10-IDEX-0002-02), and more specifically within the framework of the Cluster of Excellence MATISSE and also by the grant IPER-Nano2 (ANR-18CE30-0023-01), Copin (ANR-19-CE24-0022), Frontal (ANR-19-CE09-0017), Graskop (ANR-19-CE09-0026) and NITQuantum (ANR-20-ASTR-0008-01), Bright (ANR-21-CE24-0012-02), MixDferro (ANR-21-CE09-0029) and Quicktera (ANR-22-CE09-0018).

Data Availability Statement

The data used to support the findings of this study are included within the article and its supplementary informations.

REFERENCES

1. Wang, Y.; Gu, Y.; Cui, A.; Li, Q.; He, T.; Zhang, K.; Wang, Z.; Li, Z.; Zhang, Z.; Wu, P.; et al. Fast Uncooled Mid-Wavelength Infrared Photodetectors with Heterostructures of van Der Waals on Epitaxial HgCdTe. *Advanced Materials* **2022**, *34*, 2107772, doi:10.1002/adma.202107772.
2. Lu, H.; Carroll, G.M.; Neale, N.R.; Beard, M.C. Infrared Quantum Dots: Progress, Challenges, and Opportunities. *ACS Nano* **2019**, *13*, 939–953, doi:10.1021/acsnano.8b09815.
3. Rogalski, A. Progress in Quantum Dot Infrared Photodetectors. In *Quantum Dot Photodetectors*; Tong, X., Wu, J., Wang, Z.M., Eds.; Lecture Notes in Nanoscale Science and Technology; Springer International Publishing: Cham, 2021; pp. 1–74 ISBN 978-3-030-74270-6.
4. Pradhan, S.; Di Stasio, F.; Bi, Y.; Gupta, S.; Christodoulou, S.; Stavrinadis, A.; Konstantatos, G. High-Efficiency Colloidal Quantum Dot Infrared Light-Emitting Diodes via Engineering at the Supra-Nanocrystalline Level. *Nature Nanotech* **2019**, *14*, 72–79, doi:10.1038/s41565-018-0312-y.
5. Qu, J.; Weis, M.; Izquierdo, E.; Mizrahi, S.G.; Chu, A.; Dabard, C.; Gréboval, C.; Bossavit, E.; Prado, Y.; Péronne, E.; et al. Electroluminescence from Nanocrystals above 2 Mm. *Nat. Photon.* **2022**, *16*, 38–44, doi:10.1038/s41566-021-00902-y.

6. Sayevich, V.; Robinson, Z.L.; Kim, Y.; Kozlov, O.V.; Jung, H.; Nakotte, T.; Park, Y.-S.; Klimov, V.I. Highly Versatile Near-Infrared Emitters Based on an Atomically Defined HgS Interlayer Embedded into a CdSe/CdS Quantum Dot. *Nat. Nanotechnol.* **2021**, *16*, 673–679, doi:10.1038/s41565-021-00871-x.
7. Geiregat, P.; Houtepen, A.J.; Sagar, L.K.; Infante, I.; Zapata, F.; Grigel, V.; Allan, G.; Delerue, C.; Van Thourhout, D.; Hens, Z. Continuous-Wave Infrared Optical Gain and Amplified Spontaneous Emission at Ultralow Threshold by Colloidal HgTe Quantum Dots. *Nature Mater* **2018**, *17*, 35–42, doi:10.1038/nmat5000.
8. Cryer, M.E.; Browning, L.A.; Plank, N.O.V.; Halpert, J.E. Large Photogain in Multicolor Nanocrystal Photodetector Arrays Enabling Room-Temperature Detection of Targets Above 100 °C. *ACS Photonics* **2020**, *7*, 3078–3085, doi:10.1021/acsphotonics.0c01156.
9. Chen, M.; Lu, H.; Abdelazim, N.M.; Zhu, Y.; Wang, Z.; Ren, W.; Kershaw, S.V.; Rogach, A.L.; Zhao, N. Mercury Telluride Quantum Dot Based Phototransistor Enabling High-Sensitivity Room-Temperature Photodetection at 2000 Nm. *ACS Nano* **2017**, *11*, 5614–5622, doi:10.1021/acsnano.7b00972.
10. Dong, Y.; Chen, M.; Yiu, W.K.; Zhu, Q.; Zhou, G.; Kershaw, S.V.; Ke, N.; Wong, C.P.; Rogach, A.L.; Zhao, N. Solution Processed Hybrid Polymer: HgTe Quantum Dot Phototransistor with High Sensitivity and Fast Infrared Response up to 2400 Nm at Room Temperature. *Advanced Science* **2020**, *7*, 2000068, doi:10.1002/advs.202000068.
11. Bossavit, E.; Qu, J.; Abadie, C.; Dabard, C.; Dang, T.; Izquierdo, E.; Khalili, A.; Gréboval, C.; Chu, A.; Pierini, S.; et al. Optimized Infrared LED and Its Use in an All-HgTe Nanocrystal-Based Active Imaging Setup. *Advanced Optical Materials n/a*, 2101755, doi:10.1002/adom.202101755.
12. Pejović, V.; Georgitzikis, E.; Lee, J.; Lieberman, I.; Cheyns, D.; Heremans, P.; Malinowski, P.E. Infrared Colloidal Quantum Dot Image Sensors. *IEEE Transactions on Electron Devices* **2021**, 1–11, doi:10.1109/TED.2021.3133191.
13. Erwin, S.C.; Zu, L.; Haftel, M.I.; Efros, A.L.; Kennedy, T.A.; Norris, D.J. Doping Semiconductor Nanocrystals. *Nature* **2005**, *436*, 91–94, doi:10.1038/nature03832.
14. Talapin, D.V.; Murray, C.B. PbSe Nanocrystal Solids for N- and p-Channel Thin Film Field-Effect Transistors. *Science* **2005**, *310*, 86–89, doi:10.1126/science.1116703.
15. Shulga, A.G.; Kahmann, S.; Dirin, D.N.; Graf, A.; Zaumseil, J.; Kovalenko, M.V.; Loi, M.A. Electroluminescence Generation in PbS Quantum Dot Light-Emitting Field-Effect Transistors with Solid-State Gating. *ACS Nano* **2018**, *12*, 12805–12813, doi:10.1021/acsnano.8b07938.
16. Lan, X.; Chen, M.; Hudson, M.H.; Kamysbayev, V.; Wang, Y.; Guyot-Sionnest, P.; Talapin, D.V. Quantum Dot Solids Showing State-Resolved Band-like Transport. *Nat Mater* **2020**, *19*, 323–329, doi:10.1038/s41563-019-0582-2.
17. Lhuillier, E.; Keuleyan, S.; Zolotavin, P.; Guyot-Sionnest, P. Mid-Infrared HgTe/As2S3 Field Effect Transistors and Photodetectors. *Advanced Materials* **2013**, *25*, 137–141, doi:10.1002/adma.201203012.
18. Chung, D.S.; Lee, J.-S.; Huang, J.; Nag, A.; Ithurria, S.; Talapin, D.V. Low Voltage, Hysteresis Free, and High Mobility Transistors from All-Inorganic Colloidal Nanocrystals. *Nano Lett.* **2012**, *12*, 1813–1820, doi:10.1021/nl203949n.
19. Lim, B.T.; Cho, J.; Cheon, K.H.; Sim, K.M.; Shin, K.; Chung, D.S. Zirconium Oxide Dielectric Layer Grown by a Surface Sol–Gel Method for Low-Voltage, Hysteresis-Free, and High-Mobility Polymer Field Effect Transistors. *Organic Electronics* **2016**, *28*, 1–5, doi:10.1016/j.orgel.2015.10.008.
20. Kim, H.; Cho, K.; Kim, D.W.; Lee, H.R.; Kim, S. Bottom- and Top-Gate Field-Effect Thin-Film Transistors with p Channels of Sintered HgTe Nanocrystals. *Applied Physics Letters* **2006**, *89*, doi:10.1063/1.2364153.
21. Kim, D.-W.; Jang, J.; Kim, H.; Cho, K.; Kim, S. Electrical Characteristics of HgTe Nanocrystal-Based Thin Film Transistors Fabricated on Flexible Plastic Substrates. *Thin Solid Films* **2008**, *516*, 7715–7719, doi:10.1016/j.tsf.2008.04.044.
22. Gréboval, C.; Dabard, C.; Konstantinov, N.; Cavallo, M.; Chee, S.-S.; Chu, A.; Dang, T.H.; Khalili, A.; Izquierdo, E.; Prado, Y.; et al. Split-Gate Photodiode Based on Graphene/HgTe

Heterostructures with a Few Nanosecond Photoresponse. *ACS Appl. Electron. Mater.* **2021**, *3*, 4681–4688, doi:10.1021/acsaelm.1c00442.
23. Chee, S.-S.; Gréboval, C.; Magalhaes, D.V.; Ramade, J.; Chu, A.; Qu, J.; Rastogi, P.; Khalili, A.; Dang, T.H.; Dabard, C.; et al. Correlating Structure and Detection Properties in HgTe Nanocrystal Films. *Nano Lett.* **2021**, *21*, 4145–4151, doi:10.1021/acs.nanolett.0c04346.
24. Shulga, A.G.; Piveteau, L.; Bisri, S.Z.; Kovalenko, M.V.; Loi, M.A. Double Gate PbS Quantum Dot Field-Effect Transistors for Tuneable Electrical Characteristics. *Advanced Electronic Materials* **2016**, *2*, 1500467, doi:10.1002/aelm.201500467.
25. Gréboval, C.; Chu, A.; Magalhaes, D.V.; Ramade, J.; Qu, J.; Rastogi, P.; Khalili, A.; Chee, S.-S.; Aubin, H.; Vincent, G.; et al. Ferroelectric Gating of Narrow Band-Gap Nanocrystal Arrays with Enhanced Light–Matter Coupling. *ACS Photonics* **2021**, *8*, 259–268, doi:10.1021/acsphotonics.0c01464.
26. Liu, H.; Keuleyan, S.; Guyot-Sionnest, P. N- and p-Type HgTe Quantum Dot Films. *J. Phys. Chem. C* **2012**, *116*, 1344–1349, doi:10.1021/jp2109169.
27. Livache, C.; Izquierdo, E.; Martinez, B.; Dufour, M.; Pierucci, D.; Keuleyan, S.; Cruguel, H.; Becerra, L.; Fave, J.L.; Aubin, H.; et al. Charge Dynamics and Optolectronic Properties in HgTe Colloidal Quantum Wells. *Nano Lett.* **2017**, *17*, 4067–4074, doi:10.1021/acs.nanolett.7b00683.
28. Houtepen, A.J.; Vanmaekelbergh, D. Orbital Occupation in Electron-Charged CdSe Quantum-Dot Solids. *J. Phys. Chem. B* **2005**, *109*, 19634–19642, doi:10.1021/jp053103i.
29. L. Roest, A.; J. Houtepen, A.; J. Kelly, J.; Vanmaekelbergh, D. Electron-Conducting Quantum-Dot Solids with Ionic Charge Compensation. *Faraday Discussions* **2004**, *125*, 55–62, doi:10.1039/B302839A.
30. Mulder, J.T.; du Fossé, I.; Alimoradi Jazi, M.; Manna, L.; Houtepen, A.J. Electrochemical P-Doping of CsPbBr3 Perovskite Nanocrystals. *ACS Energy Lett.* **2021**, *6*, 2519–2525, doi:10.1021/acsenergylett.1c00970.
31. Noumbé, U.N.; Gréboval, C.; Livache, C.; Chu, A.; Majjad, H.; Parra López, L.E.; Mouafo, L.D.N.; Doudin, B.; Berciaud, S.; Chaste, J.; et al. Reconfigurable 2D/0D p–n Graphene/HgTe Nanocrystal Heterostructure for Infrared Detection. *ACS Nano* **2020**, *14*, 4567–4576, doi:10.1021/acsnano.0c00103.
32. Gréboval, C.; Noumbe, U.; Goubet, N.; Livache, C.; Ramade, J.; Qu, J.; Chu, A.; Martinez, B.; Prado, Y.; Ithurria, S.; et al. Field-Effect Transistor and Photo-Transistor of Narrow-Band-Gap Nanocrystal Arrays Using Ionic Glasses. *Nano Lett.* **2019**, *19*, 3981–3986, doi:10.1021/acs.nanolett.9b01305.
33. Gréboval, C.; Noumbé, U.N.; Chu, A.; Prado, Y.; Khalili, A.; Dabard, C.; Dang, T.H.; Colis, S.; Chaste, J.; Ouerghi, A.; et al. Gate Tunable Vertical Geometry Phototransistor Based on Infrared HgTe Nanocrystals. *Appl. Phys. Lett.* **2020**, *117*, 251104, doi:10.1063/5.0032622.
34. Wang, H.; Liu, Q.; Feng, X.; Zhang, Z.; Wang, K.; Liu, Z.; Dai, J.-F. An Ambipolar Transistor Based on a Monolayer WS2 Using Lithium Ions Injection. *Mater. Res. Express* **2020**, *7*, 076302, doi:10.1088/2053-1591/aba395.
35. Philippi, M.; Gutiérrez-Lezama, I.; Ubrig, N.; Morpurgo, A.F. Lithium-Ion Conducting Glass Ceramics for Electrostatic Gating. *Appl. Phys. Lett.* **2018**, *113*, 033502, doi:10.1063/1.5038407.
36. Zhao, J.; Wang, M.; Li, H.; Zhang, X.; You, L.; Qiao, S.; Gao, B.; Xie, X.; Jiang, M. Lithium-Ion-Based Solid Electrolyte Tuning of the Carrier Density in Graphene. *Sci Rep* **2016**, *6*, 34816, doi:10.1038/srep34816.
37. Alam, M.H.; Xu, Z.; Chowdhury, S.; Jiang, Z.; Taneja, D.; Banerjee, S.K.; Lai, K.; Braga, M.H.; Akinwande, D. Lithium-Ion Electrolytic Substrates for Sub-1V High-Performance Transition Metal Dichalcogenide Transistors and Amplifiers. *Nat Commun* **2020**, *11*, 3203, doi:10.1038/s41467-020-17006-w.
38. Zhu, C.S.; Cui, J.H.; Lei, B.; Wang, N.Z.; Shang, C.; Meng, F.B.; Ma, L.K.; Luo, X.G.; Wu, T.; Sun, Z.; et al. Tuning Electronic Properties of $FeSe_{0.5}Te_{0.5}$ Thin Flakes Using a Solid Ion Conductor Field-Effect Transistor. *Phys. Rev. B* **2017**, *95*, 174513, doi:10.1103/PhysRevB.95.174513.
39. Gréboval, C.; Chu, A.; Goubet, N.; Livache, C.; Ithurria, S.; Lhuillier, E. Mercury Chalcogenide Quantum Dots: Material Perspective for Device Integration. *Chem. Rev.* **2021**, *121*, 3627–3700, doi:10.1021/acs.chemrev.0c01120.

40. Olmon, R.L.; Slovick, B.; Johnson, T.W.; Shelton, D.; Oh, S.-H.; Boreman, G.D.; Raschke, M.B. Optical Dielectric Function of Gold. *Phys. Rev. B* **2012**, *86*, 235147, doi:10.1103/PhysRevB.86.235147.
41. Rastogi, P.; Chu, A.; Dang, T.H.; Prado, Y.; Gréboval, C.; Qu, J.; Dabard, C.; Khalili, A.; Dandeu, E.; Fix, B.; et al. Complex Optical Index of HgTe Nanocrystal Infrared Thin Films and Its Use for Short Wave Infrared Photodiode Design. *Advanced Optical Materials* **2021**, *9*, 2002066, doi:10.1002/adom.202002066.
42. Keuleyan, S.; Lhuillier, E.; Guyot-Sionnest, P. Synthesis of Colloidal HgTe Quantum Dots for Narrow Mid-IR Emission and Detection. *J. Am. Chem. Soc.* **2011**, *133*, 16422–16424, doi:10.1021/ja2079509.
43. Martinez, B.; Ramade, J.; Livache, C.; Goubet, N.; Chu, A.; Gréboval, C.; Qu, J.; Watkins, W.L.; Becerra, L.; Dandeu, E.; et al. HgTe Nanocrystal Inks for Extended Short-Wave Infrared Detection. *Advanced Optical Materials* **2019**, *7*, 1900348, doi:10.1002/adom.201900348.
44. Lhuillier, E.; Robin, A.; Ithurria, S.; Aubin, H.; Dubertret, B. Electrolyte-Gated Colloidal Nanoplatelets-Based Phototransistor and Its Use for Bicolor Detection. *Nano Lett.* **2014**, *14*, 2715–2719, doi:10.1021/nl5006383.
45. Lhuillier, E.; Keuleyan, S.; Guyot-Sionnest, P. Optical Properties of HgTe Colloidal Quantum Dots. *Nanotechnology* **2012**, *23*, 175705, doi:10.1088/0957-4484/23/17/175705.
46. Chen, M.; Lu, L.; Yu, H.; Li, C.; Zhao, N. Integration of Colloidal Quantum Dots with Photonic Structures for Optoelectronic and Optical Devices. *Advanced Science* **2021**, *8*, 2101560, doi:10.1002/advs.202101560.
47. Maës, C.; Vincent, G.; Flores, F.G.-P.; Cerutti, L.; Haïdar, R.; Taliercio, T. Infrared Spectral Filter Based on All-Semiconductor Guided-Mode Resonance. *Opt. Lett., OL* **2019**, *44*, 3090–3093, doi:10.1364/OL.44.003090.
48. Sharon, A.; Rosenblatt, D.; Friesem, A.A. Resonant Grating–Waveguide Structures for Visible and near-Infrared Radiation. *J. Opt. Soc. Am. A, JOSAA* **1997**, *14*, 2985–2993, doi:10.1364/JOSAA.14.002985.
49. Chu, A.; Gréboval, C.; Goubet, N.; Martinez, B.; Livache, C.; Qu, J.; Rastogi, P.; Bresciani, F.A.; Prado, Y.; Suffit, S.; et al. Near Unity Absorption in Nanocrystal Based Short Wave Infrared Photodetectors Using Guided Mode Resonators. *ACS Photonics* **2019**, *6*, 2553–2561, doi:10.1021/acsphotonics.9b01015.
50. Moghaddam, N.; Gréboval, C.; Qu, J.; Chu, A.; Rastogi, P.; Livache, C.; Khalili, A.; Xu, X.Z.; Baptiste, B.; Klotz, S.; et al. The Strong Confinement Regime in HgTe Two-Dimensional Nanoplatelets. *J. Phys. Chem. C* **2020**, *124*, 23460–23468, doi:10.1021/acs.jpcc.0c07533.
51. Guo, N.; Xiao, L.; Gong, F.; Luo, M.; Wang, F.; Jia, Y.; Chang, H.; Liu, J.; Li, Q.; Wu, Y.; et al. Light-Driven WSe_2 -ZnO Junction Field-Effect Transistors for High-Performance Photodetection. *Adv. Sci.* **2020**, *7*, 1901637, doi:10.1002/advs.201901637.
52. Konstantatos, G.; Sargent, E.H. PbS Colloidal Quantum Dot Photoconductive Photodetectors: Transport, Traps, and Gain. *Appl. Phys. Lett.* **2007**, *91*, 173505, doi:10.1063/1.2800805.
53. Chu, A.; Gréboval, C.; Prado, Y.; Majjad, H.; Delerue, C.; Dayen, J.-F.; Vincent, G.; Lhuillier, E. Infrared Photoconduction at the Diffusion Length Limit in HgTe Nanocrystal Arrays. *Nat Commun* **2021**, *12*, 1794, doi:10.1038/s41467-021-21959-x.
54. Liu, H.; Lhuillier, E.; Guyot-Sionnest, P. 1/f Noise in Semiconductor and Metal Nanocrystal Solids. *Journal of Applied Physics* **2014**, *115*, 154309, doi:10.1063/1.4871682.
55. Lai, Y.; Li, H.; Kim, D.K.; Diroll, B.T.; Murray, C.B.; Kagan, C.R. Low-Frequency (1/f) Noise in Nanocrystal Field-Effect Transistors. *ACS Nano* **2014**, *8*, 9664–9672, doi:10.1021/nn504303b.

TOC graphic

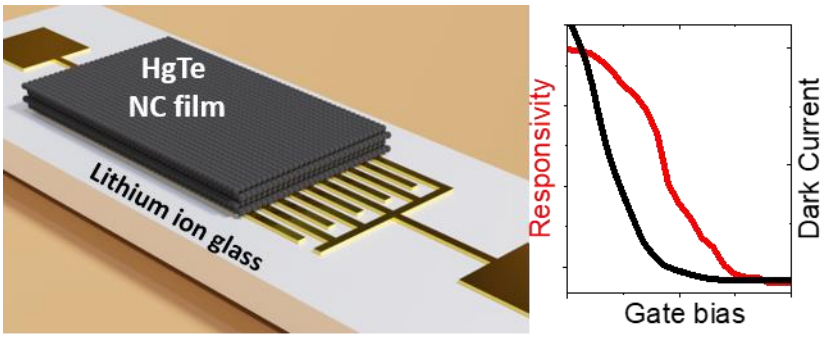
HgTe
NC film
Lithium ion glass
Responsivity
Dark Current
Gate bias